Generation of Mars Helicopter Rotor Model for Comprehensive Analyses

Witold J. F. Koning
Science and Technology Corporation
NASA Ames Research Center
Moffett Field, California
witold.koning@nasa.gov

Wayne Johnson
NASA Ames Research Center
Moffett Field, California
wayne.johnson@nasa.gov

Brian G. Allan
NASA Langley Research Center
Hampton, Virginia
brian.g.allan@nasa.gov

ABSTRACT[1]

The present research is aimed at providing a performance model for the Mars Helicopter (MH), to understand the complexity of the flow, and identify future regions of flow simulation improvement. The low density of the Martian atmosphere and the relatively small MH rotor, result in very low chord-based Reynolds number flows ($Re_c \approx 10^3$ to $Re_c \approx 10^4$). The low density and low Reynolds numbers reduce the lifting force and lifting efficiency, respectively. The high drag coefficients in subcritical flow, especially for thicker sections, are attributed to laminar separation from the rear of the airfoil. In the absence of test data, efforts have been made to explore these effects using prior very low Reynolds number research efforts. The rotor chord-based Reynolds number range is observed to be subcritical, which makes boundary layer transition unlikely to occur. The state of the two-dimensional rotor boundary layer in hover is approximated by calculating the instability point, laminar separation point, and the transition location to provide understanding of the flow state in the high Mach-low Reynolds number regime. The results are then used to investigate the need for turbulence modeling in Computational Fluid Dynamics (CFD) calculations. The goal is to generate a performance model for the MH rotor for a free wake analysis because of the low cost for design. In this study, a Reynolds-Averaged Navier-Stokes (RANS) based approach is used to generate the airfoil deck using C81Gen with experimental data for very high angles of attack. A full Grid Resolution Study is performed and over 4,500 cases are completed to create the full airfoil deck. The laminar separation locations are predicted within the accuracy of the approximate method when compared with the CFD calculations. The model is presented through airfoil data tables (c81 files) that are used by comprehensive rotor analysis codes such as CAMRADII or the mid-fidelity CFD solver RotCFD. Finally, the rotor performance is compared with experimental data from the 25ft Space Simulator at the NASA Jet Propulsion Laboratory (JPL) and shows good correlation for the rotor Figure of Merit over the available thrust range.

NOMENCLATURE

c	airfoil chord	n	amplification factor
c_d	section drag coefficient	p	pressure
c_l	section lift coefficient	r	approximate roughness factor; rotor radial coordinate
c_m	section moment coefficient		
c'	total airfoil contour length (leading to trailing edge)	R	gas constant; rotor radius
		Re	Reynolds number
g	gravitational acceleration	Re_{crit}	critical Reynolds number
M	Mach number	s	airfoil contour length (from leading edge)
M_∞	freestream Mach number		

[1] *Presented at the AHS Specialists' Conference on Aeromechanics Design for Transformative Vertical Flight, San Francisco, California, USA, January 16-18, 2018.*

T	temperature
t	airfoil thickness
U	velocity
U_∞	freestream velocity
U_m	velocity obtained from potential flow solution
x_{min}	point of minimum pressure
x, y	rectangular coordinates in the plane
α	angle of attack
α	wave number
β	Hartree beta
β_i	amplification (or damping) factor
β_r	circular frequency of disturbance
δ	boundary layer thickness
δ_1, δ^*	boundary layer displacement thickness
δ_2	boundary layer momentum thickness
ε_{ct}	chordline twist
γ	specific heat ratio
Λ	boundary layer shape factor
Λ_{P4}	boundary layer shape factor (LP4 method)
μ	dynamic viscosity
ν	kinematic viscosity
ρ	density
ρ_∞	freestream density
σ	standard deviation
σ	rotor solidity
τ_0	shear stress

ABBREVIATIONS

ARC2D	Two-Dimensional Navier-Stokes Flow Solver
BL	Boundary Layer
C81Gen	C81 Generator
CAMRADII	Comprehensive Analytical Model of Rotorcraft Aerodynamics and Dynamics
CFD	Computational Fluid Dynamics
DNS	Direct Numerical Simulation
FM	Figure of Merit
GRS	Grid Resolution Study
JPL	Jet Propulsion Laboratory
LE	Leading Edge
LSB	Laminar Separation Bubble
MAV	Micro Aerial Vehicle
MH	Mars Helicopter
P	Pressure side of airfoil
RANS	Reynolds-Averaged Navier-Stokes
RotCFD	Rotorcraft CFD
S	Suction side of airfoil
TE	Trailing Edge
TS	Tollmien-Schlichting (waves)
UAV	Unmanned Aerial Vehicle
VTOL	Vertical Take-Off and Landing

INTRODUCTION

The NASA Jet Propulsion Laboratory (JPL) designed the Mars Helicopter (MH) in collaboration with AeroVironment Inc., NASA Ames Research Center, and NASA Langley Research Center to explore the possibility of a Vertical Take-Off and Landing (VTOL) Unmanned Aerial Vehicle (UAV) for flight on Mars. It serves as a technology demonstrator, eventually intended to perform low-altitude flight in the Martian atmosphere.

The Martian environment provides major challenges for the design of the UAV. In 2014, Balaram et al. published an initial paper describing the conceptual design of the current Mars Helicopter [1]. More recent, Grip et al. published a paper describing the flight dynamics of the MH and experimental testing in the 25-ft Space Simulator at JPL [2]. Balaram et al. describe the key design features and results from a full-scale prototype [3].

The design of the UAV is a solar powered co-axial helicopter with a mass of roughly 1.8 kg and a 1.21 m rotor diameter. The helicopter is battery powered with an endurance allowing up to 90 s flights that will be conducted fully autonomously because of the communication delay between Earth and Mars.

MARS ATMOSPHERIC CONDITIONS

The low density Martian atmosphere and the relatively small MH rotor result in very low chord-based Reynolds number flows over a range of $Re_c \approx 10^3$ to 10^4. Furthermore, the low density and low Reynolds number reduce the lifting force and lifting efficiency, respectively, which are only marginally compensated by a lower gravitational acceleration of around $g = 3.71$ m/s^2. Table 1 gives an overview of the operating conditions for the three Martian Conditions (MC) under consideration in the present work.

In addition, the low temperature and largely CO_2 based atmosphere result in a low speed of sound, further constraining rotor operation in the Martian atmosphere by increasing compressibility effects.

Table 1. Operating conditions for Mars Condition 1-3

Variable	Earth SLS	MC 1	MC 2	MC 3
Density, ρ [kg/m^3]	1.225	0.015	0.017	0.020
Temperature, T [K]	288.20	248.20	223.20	193.20
Gas Constant, R [m^2/s^2/K]	287.10	188.90	188.90	188.90
Specific Heat Ratio, γ [~]	1.400	1.289	1.289	1.289
Dynamic Viscosity, μ [Ns/m^2]	$1.750{\cdot}10^{-5}$	$1.130{\cdot}10^{-5}$	$1.130{\cdot}10^{-5}$	$1.130{\cdot}10^{-5}$
Static Pressure, p [Pa]	101,300	703.10	716.60	729.70

The composition of the Martian atmosphere is 95% CO_2 with the remaining 5 percent comprised of trace gases. A seasonal variation of approximately 20% of the planetary atmospheric mass occurs on Mars due to polar CO_2 condensation and sublimation [4]. An overview of the composition of the Martian atmosphere is presented in Table A1.

MARS HELICOPTER ROTOR DESIGN

Early isolated rotor hover testing at reduced pressure was done by Young et al. [5]. The experiment was performed in a large NASA Ames environmental chamber that can be reduced to atmospheric densities and pressure representative of the Martian atmosphere. An initial attempt to predict the rotor hover performance was presented by Corfeld et al. [6].

The Mars Helicopter, shown in Figure 1, features a co-axial rotor with two counter-rotating, hingeless, two-bladed rotors. The rotors are spaced apart at approximately 12% of the rotor radius and are designed to operate at speeds up to 2,800 RPM. Flights are constrained to favorable weather with limited wind and gust speeds. The maximum airspeed is constrained to 10 m/s horizontally and 3 m/s vertically [2].

Figure 1. An artist's impression of the Mars Helicopter [7]

The airfoils for the rotor are developed by AeroVironment, Inc. Figure B1 and Figure B2 provide an overview of the blade chord, thickness, and twist distribution, and airfoil cross-sections. Table B1 shows the details of the MH airfoil thickness and camber. The clf5605 airfoil used at 3/4-span is presented in Figure 2.

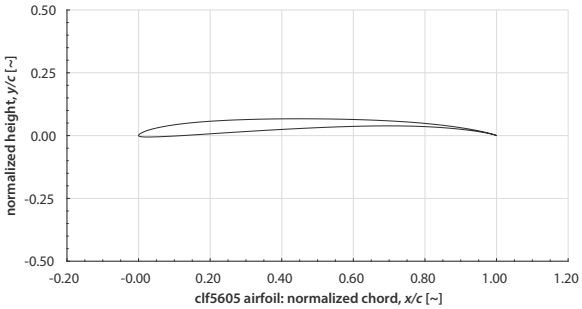

Figure 2. The clf5605 airfoil cross section at 3/4-span

Table 2 gives an overview of the blade chord, thickness, and twist distribution. No sweep is applied on the rotor blade.

Table 2. MH critical radial station selection

CFD Station	r/R [~]	c/R [~]	t/c [~]	ε_{ct} [deg]	Airfoil
Station 1	0.0908	0.0506	0.973	16.32	Station 1
Station 2	0.2000	0.1407	0.220	17.62	Station 2
Station 3	0.2950	0.1968	0.098	15.92	Station 3
Station 4	0.3903	0.1968	0.060	12.07	Station 4
Station 5	0.5271	0.1627	0.050	8.43	clf5605
Station 6	0.7621	0.1209	0.050	3.93	clf5605
Station 65	0.9241	0.0860	0.050	1.39	clf5605
Station 7	0.9912	0.0341	0.050	0.06	clf5605

CRITICAL AIRFOIL SELECTION

To generate the aerodynamic rotor model for comprehensive analyses, it is key to identify the critical airfoils along the span which are analyzed using 2D Computational Fluid Dynamics (CFD) simulations. These simulations will provide the aerodynamic coefficients of the airfoils required by the comprehensive analyses. The CFD stations are locations where spanwise changes in airfoil geometry and Reynolds number variations occur and areas where compressibility effects are expected, since comprehensive analyses rely on spanwise interpolation of the aerodynamic coefficients between these airfoils.

Figure 3 shows the spanwise Reynolds number distribution of the MH at Mars Condition 3. Although Station 65 was not originally selected as a critical radial station, it was introduced to enforce more adequate

interpolation. Figure 3 shows that Station 7 was not adequate for interpolation to Station 6 directly.

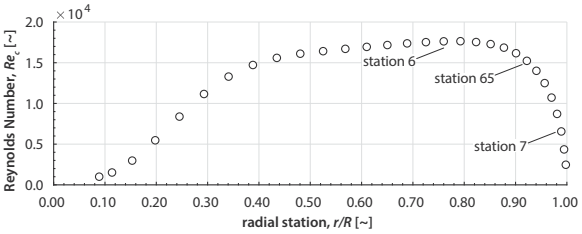

Figure 3. Reynolds number distribution for the MH rotor

The rotor model is intended to evaluate hover performance with limited forward flight speed. A select angle of attack and Mach number range is chosen for each CFD station as presented in Table 3. The angle of attack range used 1-degree increments and the Mach range uses increments equal to 0.1. Each station's alpha-Mach pair will provide the lift, drag, and moment coefficients for the c81 airfoil deck files required for the comprehensive analyses.

Table 3. c81 alpha-Mach pair input parameters

CFD station	Airfoil	α [deg]	M [~]
Station 1	Station 1	-15 to 20	0.10 to 0.30
Station 2	Station 2	-15 to 20	0.10 to 0.40
Station 3	Station 3	-15 to 20	0.10 to 0.50
Station 4	Station 4	-15 to 20	0.10 to 0.50
Station 5	clf5605	-15 to 20	0.20 to 0.50
Station 6	clf5605	-15 to 20	0.20 to 0.70
Station 65	clf5605	-15 to 20	0.20 to 0.85
Station 7	clf5605	-15 to 20	0.20 to 0.90

LOW REYNOLDS NUMBER RESEARCH EFFORTS

The MH rotor chord-based Reynolds number are in the range $Re_c \approx 10^3$ to 10^4. This range of Reynolds numbers will be used synonymously with 'low Reynolds numbers' in this paper. Airfoil performance at these low Reynolds number is not well understood [8]. For Earth-based research Micro Aerial Vehicles (MAV), insects, and bird flight fall in this Reynolds number range [9].

Most research on airfoils emanates from high-speed transport and low speed aircraft. The most common range of research along the Reynolds number-Mach range has been indicated in Figure 4. The Reynolds number Mach pairs for each discrete Mach number to be simulated (see Table 3) have been plotted for each CFD station of the MH rotor. The estimated Reynolds number-Mach points in hover at 3/4-span for two commercial (Earth-based) quadcopters, the DJI Phantom and the SUI Endurance, have been added for reference[2]. The Reynolds number for the MH and noted quadcopters is the Reynolds number found on the chord of the rotor.

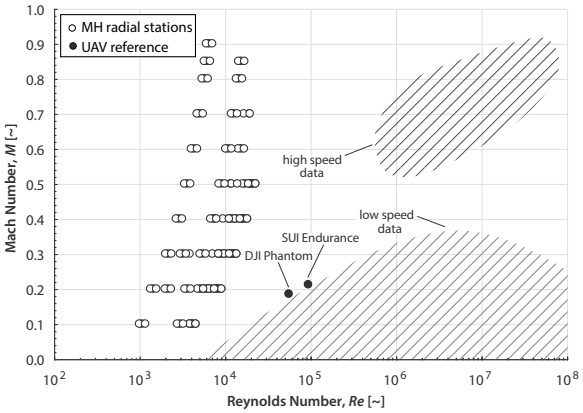

Figure 4. General Mach-Reynolds number research areas (created referring to [10]–[12])

Despite the scarcity of research on (very) low Reynolds number flows, several valuable references were identified. Hoerner provides a multitude of low Reynolds number empirical references [13], [14]. Schmitz elaborates on model airplane aerodynamics and tunnel test considerations [15]. Bussmann and Ulrich investigate boundary layer instability and compare experimental and analytical laminar separation locations [16]. McMasters and Henderson discuss low-speed airfoil synthesis [10], and Mueller writes extensively on wing aerodynamics for MAV applications [17]. The recent interest in Martian (or planetary) atmospheric flight resulted in various research efforts on low Reynolds number design [6], [12].

BOUNDARY-LAYER TRANSITION

At very low Reynolds Numbers the flow state can be subcritical. In a subcritical flow state the boundary layer is fully laminar on the airfoil; in supercritical state it exhibits (partially) turbulent flow. The flow state is only called subcritical if laminar flow exists for the whole range of angles

[2] *C. Russell, NASA Ames Research Center, personal communication, 2017.*

of attack. The Reynolds number at which laminar flow over an airfoil just begins to exhibit turbulent features is the critical Reynolds number, Re_{crit}. In the context of this paper 'critical' is unrelated to the flow properties at sonic conditions. Figure 5 shows the general trend of the transition location with lowering Reynolds number from various experimental results.

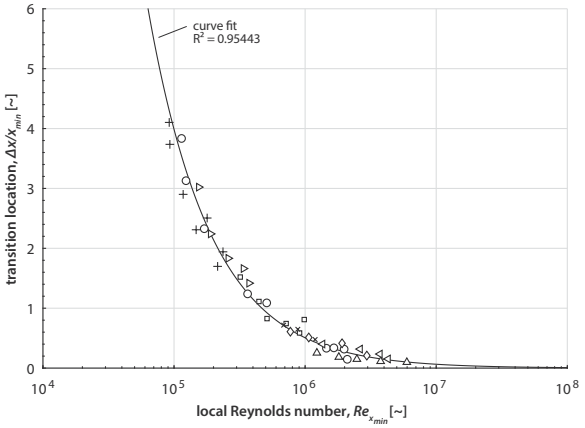

Figure 5. Statistical evaluation of transition location (reproduced from Hoerner [13])

The transition location is expressed as the ratio of the location of transition, Δx, with the point of minimum pressure, x_{min}. The point of minimum pressure needs to be forward to keep transition at low Reynolds numbers. This is avoided on laminar airfoil designs for low Reynolds numbers to keep long stretches of laminar flow and to delay the start of the adverse pressure gradient.

SUBCRITICAL REYNOLDS NUMBER FLOW

Airfoils at very low Reynolds numbers are subject to the growth of thick boundary layers. The most apparent effect on performance of operation at very low Reynolds numbers is a large increase in section drag coefficient. Zero lift drag coefficients for airfoils range from $c_d = 0.03$ to 0.08 depending on the Reynolds number and geometry [17].

Hoerner collected data on sectional drag of various streamlined shapes at very low Reynolds numbers [13]. Figure 6 shows a summary of that data, replacing the individual experiment data points with lines at constant airfoil thickness for clarity. A clear change in Reynolds number dependency of the section drag is observed between $Re_c \approx 10^5$ to 10^6. This is the critical Reynolds number transition region where the boundary layer first starts to exhibit turbulent features. The drag coefficients for various thickness ratios are obtained for lift coefficients close to zero. Therefore, these drag values should be indicative of the minimum drag coefficient and clearly shows the increase in drag of roughly an order of magnitude when operating in the subcritical flow state compared to the supercritical state. The critical Reynolds number is around $Re_c = 10^5$ for slender streamline shapes [13]. Based on the MH airfoils of interest and their associated Reynolds number range it is likely that the MH airfoils operate in a subcritical flow state.

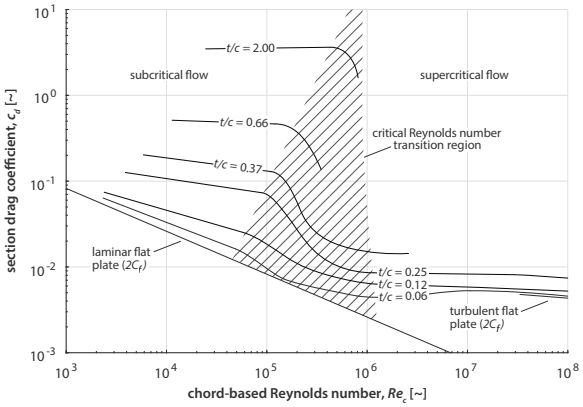

Figure 6. Reynolds number criticality based on thickness (close to zero section lift, reproduced from Hoerner [13])

The large drag increase is attributed to separation of the laminar boundary layer in the absence of boundary layer transition to turbulence [12]. A turbulent boundary layer will normally yield increased skin friction, but will delay the onset of stall due to the increased momentum of the boundary layer, usually resulting in a net reduction in drag. The laminar boundary layer is, however, unable to sustain an adverse pressure gradient very long and is likely to separate. This results in possible flow separation, even at low angles of attack. Airfoils in this regime can operate in a steady-state manner while part of the airfoil experience separated flow. Once the flow does separate, growth of the separated regions is delayed by a reduction in the Reynolds number [17].

Hoerner presents maximum lift of airfoils as function of Reynolds number for moderate

thickness and camber. The increase in drag is not reciprocated in lift to the same extent, as shown in Figure 7.

Reducing the Reynolds number leads to thicker boundary layers whose displacement effect increasingly causes an effective loss of camber with increasing angle of attack, leading to lower lift coefficients. Lift coefficients remain of order 1, resulting in a large reduction in the attainable lift-to-drag ratio in subcritical flow states [17].

The ability of these airfoils to operate in a steady-state manner, while part of the airfoil experiences separated flow, will reduce the lift curve but extend the linear range to higher angles of attack.

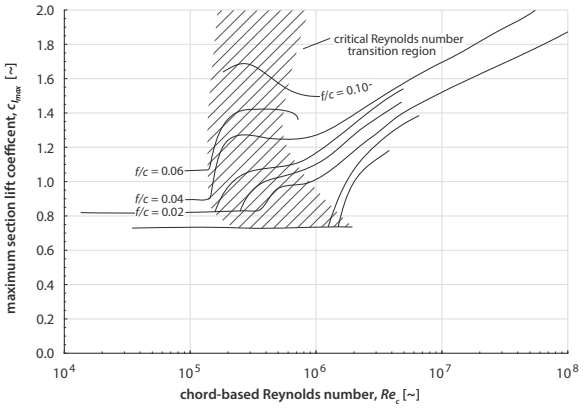

Figure 7. Maximum section lift as a function of Reynolds number ($t/c = 0.08 - 0.10$, reproduced from Hoerner [14])

Laminar airfoil designs therefore have a crest located far back which will delay the suction peak and therefore move the adverse pressure gradient towards the trailing edge, albeit only possible for a limited angle of attack range. A reduction in height of the leading edge suction peak will also reduce the adverse pressure recovery gradient and thus onset of separation [17]. Therefore, at very low Reynolds numbers, a flat plate starts performing better than smooth airfoil shapes [13], [14], [18].

LAMINAR SEPARATION AND INSTABILITY

Bussmann et al. [16] investigate the stability of the laminar boundary layer and laminar separation, both experimentally and analytically. Bussmann concludes that for constant Reynolds numbers, the instability point travels forward on the suction side and backward on the pressure side with increasing section lift coefficient. For increasing Reynolds number, the suction and pressure instability locations move forward. With increasing camber, for all lift coefficients, the instability point moves back on the suction side and forward on the pressure side.

PREDICTION OF BOUNDARY LAYER STATE

Because of the large effect of the subcritical state on the aircraft performance, it becomes important to evaluate the boundary layer state on the airfoils of the MH before the CFD analysis. Considering the goal of the present work to produce a two-dimensional airfoil deck for comprehensive analyses and to reduce the complexity of the analysis, only two-dimensional boundary layer development is investigated.

No effort has been made to investigate the effect of the periodicity of the rotor, the possibility of an unsteady boundary layer (and thus fluctuating properties regarding transition, separation etc.), or crossflows in the boundary layer.

A code is written that approximates the boundary layer development for an airfoil at a given angle of attack up to laminar separation. Subsequently, the location of boundary layer instability and transition are estimated. The aim is to be able to verify the flow state of the two-dimensional airfoils of the MH.

SEPARATION OF THE INCOMPRESSIBLE LAMINAR BOUNDARY LAYER

The momentum-integral equation for a steady, two-dimensional, incompressible boundary layer is given by [19]

$$U^2 \frac{d\delta_2}{dx} + (2\delta_2 + \delta_1) U \frac{dU}{dx} = \frac{\tau_0}{\rho}$$

The point of laminar separation is estimated using the approximate method to solve the two-dimensional boundary layer equation with pressure gradient by von Kármán and Pohlhausen [20]. The method used is the updated approach by Holstein and Bohlen [21] as presented in Schlichting's Boundary-Layer Theory [22].

The accuracy of the method in the region of an adverse pressure gradient is often low, but the ease of calculation and the approximate

requirements to observe the flow state made this approach the preferred one.

Pohlhausen assumes the fourth-degree polynomial (LP4 method) for the velocity function. The lambda shape factor

$$\Lambda_{P4} = \frac{\delta^2}{\nu}\frac{dU}{dx} = -\frac{dp}{dx}\frac{\delta}{\mu U/\delta}$$

is used in conjunction with the boundary conditions to obtain the coefficients of the polynomial. The subscript 'P4' indicates the Pohlhausen fourth degree polynomial (in contrast to the sixth-degree LP6 method). The condition $\Lambda_{P4} = 0$ occurs at a zero pressure gradient or where the potential flow experiences a local minimum or maximum. Separation occurs when $\Lambda_{P4} = -12$ (or $\Lambda = -9.63$ for the LP6 method). Holstein and Bohlen [21] introduce another set of shape factors, which Walz [23] discovers can be approximated without appreciable loss of accuracy by a linear function [22]. This is referred to as the Walz linearization from here on. The equation is integrated explicitly to yield [19]

$$\frac{U\delta_2^2}{\nu} = \frac{0.470}{U^5}\int_{x=0}^{x} U^5 dx$$

After obtaining a potential velocity distribution, this equation now allows for the direct computation of the shape factors and consequentially the point of laminar separation. The method is described extensively in Schlichtings work [19], [22] and will not be treated further.

Bussmann and Ulrich [16] follow the Pohlhausen approach to estimate the location of laminar separation. Their results are compared here with the approach of Holstein and Bohlen [21] with the linearization of the manipulated form of the momentum equation as performed by Walz [23]. Bussmann and Ulrich also compare the Pohlhausen (LP4) method with experimental findings of the location of laminar separation and show good results considering the limitations of the method.

The results by Bussmann are presented for various Joukowsky airfoils for a thickness, camber and section lift coefficient range like that expected for the MH rotor. It is noted that the Joukowsky airfoils are very similar to the MH airfoils for equal thickness and camber. Potential flow solutions are obtained from Drela's XFOIL [24] and Hepperle's JavaFoil [25]. Variation in computed angle of attack for set section lift coefficients is marginal between the two programs. The results of the analytical approximation of the Walz linearization with the reported values by Bussmann are satisfactory, as shown in Table C1. The differences are attributed to the differences in the potential flow solution.

Bussmann compares the analytical results with an experimental study. The airfoils compared had very similar camber and lift coefficients to the MH (in hover) at slightly higher thicknesses. The absolute average error expressed as the difference in normalized chord location on suction side is around 11%-chord, while on the pressure side it is 5%-chord. The laminar separation is almost exclusively predicted too early compared to experimental results. When the LP4 criterion is used, the absolute average error on the suction side dropped to 9%-chord and 4%-chord on the pressure side, as seen in Table 4. The letters S and P indicate the suction and pressure side of the airfoils, respectively. Walz's [23] linearization method is considered to be of high enough accuracy for the present investigation.

Table 4. Experimental results from Bussmann and Ulrich [16] with Walz linearization and LP4 criterion for separation

Airfoil	Source	c_l	0.00	0.25	0.50	0.75	1.00
J025	Present work	S	0.426	0.378	0.337	0.302	0.264
		P	0.424	0.470	0.525	0.574	0.639
	Experiment [16]	S	0.450	0.420	0.385	0.360	0.320
		P	0.450	0.485	0.540	0.600	0.680
J415	Present work	S	0.705	0.648	0.591	0.528	0.463
		P	0.168	0.258	0.376	0.536	N/A
	Experiment [16]	S	0.950	0.860	0.730	0.650	0.630
		P	0.190	0.290	0.310	0.330	0.480
J815	Present work	S	0.772	0.736	0.698	0.659	0.620
		P	0.042	0.054	0.084	0.135	0.218
	Experiment [16]	S	0.860	0.780	0.710	0.670	0.630
		P	0.060	0.075	0.100	0.120	0.160

NEUTRAL STABILITY FOR THE INCOMPRESSIBLE BOUNDARY LAYER

The boundary layer stability is based on existing work for the neutral stability curves. The stability of incompressible boundary layer profiles with Tollmien–Schlichting disturbances is treated by Schlichting [26] and Pretsch [27], [28]. Figure 8

shows the curves of neutral stability for laminar boundary-layer profiles and the critical Reynolds number of boundary-layer velocity profiles by Schlichting. A six-degree polynomial is used to create these calculations because the stability analysis requires a more accurate second order derivative for the mean velocity to be of use.

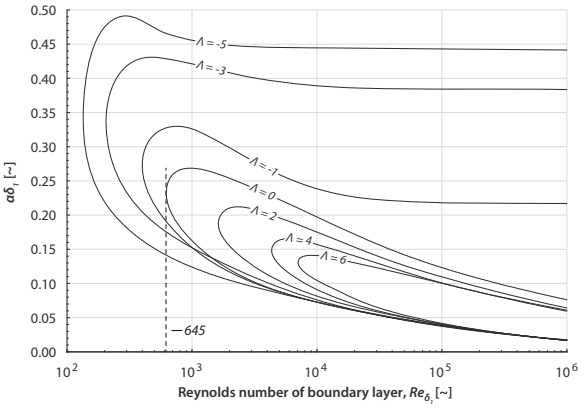

Figure 8. Curves of neutral stability for laminar boundary-layer profiles (reproduced from Schlichting [19])

The instability point is now obtained at the intersection of the critical Reynolds number with the Boundary layer Reynolds number, calculated along the airfoil profile for equal shape factors[3]. Hence, the point of instability is located at

$$\frac{U_m \delta_1}{\nu} = \left(\frac{U_m \delta_1}{\nu}\right)_{crit}$$

Wazzan et al. [29] performed a stability analysis analogous to Pretsch's work [27], [28] using a spatial instead of temporal criterion. The study indicated the finite critical Reynolds number for the separation profile, contrary to Schlichting's and Pretsch's work, as shown in Figure 9. This signifies that at (very) low Reynolds numbers, laminar separation can occur without boundary layer instability.

Wazzan's instability criterion is favorable as it encompasses the full range of shape factors from stagnation to separation, contrary to the method presented by Schlichting. Since for very low Reynolds numbers we expect to utilize the full range of velocity profiles of the boundary layer, it is preferred to utilize Wazzan's stability calculations.

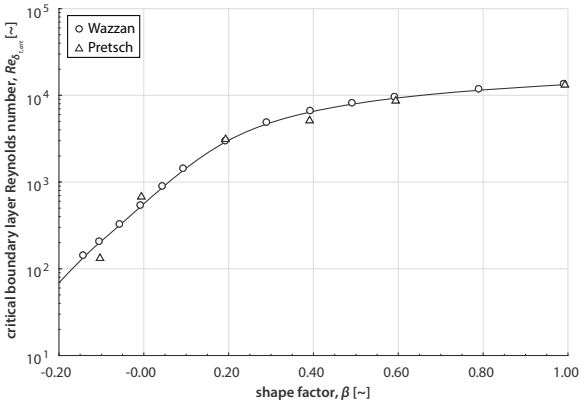

Figure 9. Effect of pressure gradient on the critical Reynolds number (reproduced from Wazzan et al. [29])

Figure 10 shows the comparison of the calculation of the limit of stability and the instability points for an elliptic cylinder with slenderness ratio $a/b = 4$ obtained from Schlichting's work and the present research.

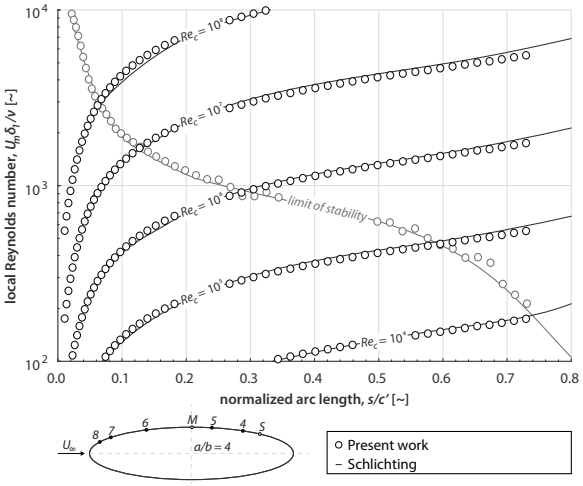

Figure 10. Calculation of the position of instability in terms of Reynolds number (created referring to Schlichting [19])

INCOMPRESSIBLE BOUNDARY LAYER TRANSITION

To exclude on-body turbulence transition for the MH rotor, it is key to investigate the onset of turbulence. There are various methods to estimate the location of transition based on local criteria or regions on the airfoil. The authors are not aware of an 'easy' method applicable at these

[3] *Wazzan et al.* [29] *question the accuracy of the stability analysis by Schlichting* [26] *referring to* [46]. *Schlichting's analysis* [26] *is, however, updated in* [19] *to use a* 6^{th} *order polynomial.*

very low Reynolds numbers. Both Schlichting [19] and Hepperle [25] describe various applied methods, although none were found satisfactory for the present research.

Assuming Tollmien-Schlichting (TS) waves are the dominant transition-initiating mechanism, the transition location, if between the instability point and laminar separation location, is calculated. Smith's work [30] shows a direct way of calculating the growth of the Tollmien-Schlichting waves from the Pretsch charts and thus the subsequent transition location.

Therefore, the analysis by Smith is used to establish the transition location by stability theory. Smith indicates the agreement is 'about average'. Amongst others, the fact that transition happens over a region and not a point further complicates the determination of a 'point'. The cumulative amplification ratio is computed as [30]

$$\int_{t_n}^{t_l} \beta_i dt = \int_{(x/c)_n}^{(x/c)_l} \frac{\beta_i \delta^*}{U} \left[\left(\frac{U}{U_\infty} \right)^3 \frac{Re_c}{{Re_{\delta^*}}^2} \right] \frac{\alpha \delta^*}{\frac{\beta_r \nu}{{U_\infty}^2}} d(x/c)$$

Using an apparent amplification of about e^9 (based on the e^n-method by van Ingen [31]) the predicted transition location did not deviate more than 18.5% from test results for two-dimensional cases [30]. The choice of the n-factor further complicates a true transition prediction. Therefore, a region can be indicated in which transition is likely to occur. Instead of the stability charts by Smith [30], the charts presented by Wazzan et al. [29] are applied because of their superior approximation of the lower bound of the critical Reynolds number.

For each chordwise location's BL shape factor, the code interpolates the stability charts as proposed by Smith and evaluates a user defined amount of chord-wise locations and frequencies. Figure 11 shows the growth of the TS waves expressed as cumulative amplification ratio for a NACA body of revolution with a fineness ratio of 9.0 [32]. The agreement is good for an amplification ratio corresponding to e^6 up to e^9. No efforts were made to match beyond these values since the slightly changed and higher-resolution charts from Wazzan et al. [29] were used in the present work and are compared to Smith's work [30]. Also, the errors in chart reading, the method of beta interpolation, differences in potential flow solutions, and limited frequency analysis in the reference all explain the differences.

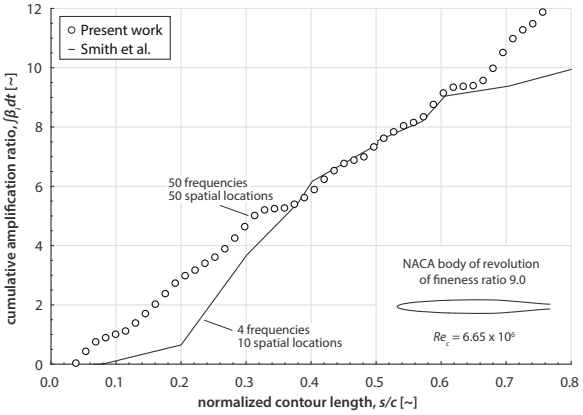

Figure 11. Growth of Tollmien-Schlichting waves for NACA body of revolution (created referring to Smith [30])

Figure 12 depicts the calculated transition curves for a NACA65 series airfoil [33] at $c_l = 0.14$. The comparison shows some deviation, for the same reasons as expressed for Figure 11.

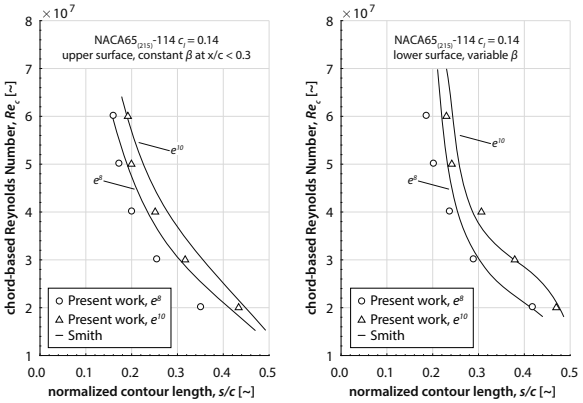

Figure 12. Calculated transition curves (created referring to Smith [30])

The code allows for a selected n-parameter from the e^n-method (i.e. the intersection of the cumulative amplification ratio with the value of e^n). Besides accounting to some degree for freestream turbulence variations, this allows the code to approximate surface roughness similarly to XFOIL [25]

$$n_{crit} = n - r$$

where r is the roughness factor (r ranges from 0 for a smooth surface to $r = 3$ for a surface with 'spots of dirt, bugs and flies'), and n is most commonly chosen as $n = 9$ [25]. When considering Martian dust storms, the accretion of dust on the rotor blades should be properly evaluated.

COMPRESSIBILITY EFFECTS ON SEPARATION, INSTABILITY, AND TRANSITION

The stability of the laminar boundary layer is directly related to the pressure gradient, which in turn is affected by compressibility. It is assumed that to estimate the influence of compressibility, the inviscid velocity distribution can be corrected for compressibility using the Karman-Tsien correction [24]

$$U = \frac{U_m(1-\lambda)}{1-\lambda(U_m/U_\infty)^2_{inc}}$$

with $\beta = \sqrt{1-M_\infty^2}$ and $\lambda = M_\infty^2/(1+\beta)^2$. This omits the evaluation and effect of temperature which would require a far more extensive calculation. Assuming adiabatic conditions, the Mach number has no effect on the stability of the laminar boundary layer but is solely dependent on the displacement-thickness Reynolds number. In addition, the amplification factor is also shown to be independent of the Mach number [34], [35].

Shockwave-boundary layer interaction is currently not investigated. Preliminary studies seem to suggest the critical Reynolds number rises with Mach number because of the shocks 'provoking' the laminar separation [19].

LAMINAR SEPARATION BUBBLES

The laminar separation bubble is frequently documented for low Reynolds number flows as they occur for wind turbines, high altitude flight and UAVs or MAVs. A thorough overview of Reynolds number regimes is presented by Carmichael [36].

Under certain circumstances, laminar separation can transition to turbulence off body and subsequently reattach. The process of separation, transition and reattachment can result in a laminar separation bubble (LSB) [9], [37]. A sketch of the generic flow structure of an LSB is shown in Figure 13.

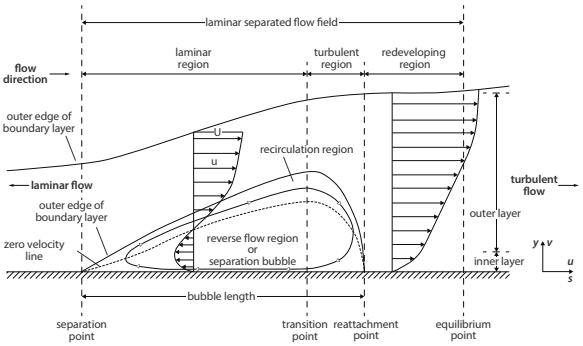

Figure 13. Sketch of flowfield with a laminar separation bubble (reproduced from Carmichael [36])

Saxena [9] observes for a SD7003 airfoil the subcritical zone; the LSB shows important effects on the pressure distribution at $Re_c = 4 \cdot 10^4$, but this effect is completely gone when Re_c lowers to $Re_c = 2 \cdot 10^4$ because the boundary layer separates completely, with no observed reattachment, as shown in Figure 14.

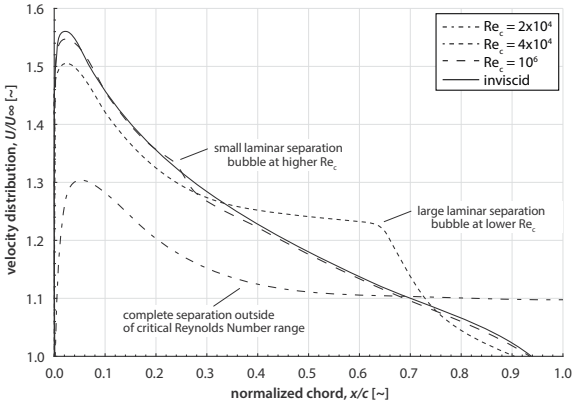

Figure 14. Upper surface velocity distribution over SD7003 airfoil at $\alpha = 4$ for various Reynolds numbers (reproduced from Saxena [38])

A closed bubble will not have large influences on lift, but could affect drag in a negative way. The generic Reynolds number effects on drag, as shown in Figure 6, indeed suggests that the SD7003 airfoil (maximum thickness around 8%) at $Re_c = 4 \cdot 10^4$ is close to the lower boundary of the critical Reynolds number transition region, even though the lift coefficient is higher (approximately $c_l \approx 0.7$).

True subcritical flow, in the definition, however, has no turbulent boundary layer. Carmichael indicates an LSB can occur between roughly $5 \cdot 10^4 < Re_c < 4 \cdot 10^6$. Furthermore, the boundary layer Reynolds number at separation

must exceed $Re_{\delta*} > 500$ for a short bubble to form. For lower values, a bubble, if occurring, is long with reattachment unlikely [36].

Huang et al. [39] obtain experimental characteristic flow modes of an NACA 0012 airfoil, reproduced in Figure 15. A clear region is observed where no separation bubble is present at $Re_c < 2 \cdot 10^4$.

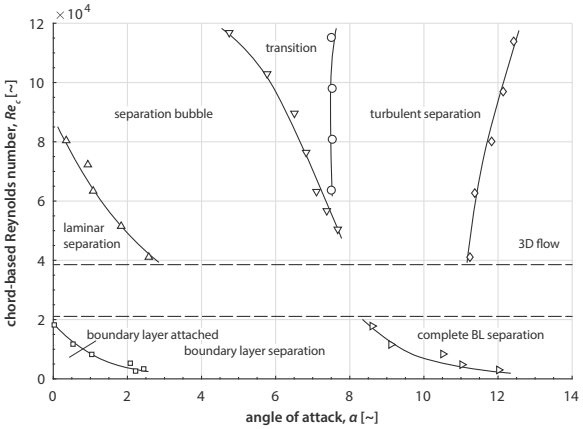

Figure 15. Regions of characteristic flow modes of an NACA 0012 airfoil (reproduced from Huang et al. [39])

Reattachment depends mostly on the Reynolds number and angle of attack. Yarusevych et al. [40] provide an overview of LSB studies and indicate that the roll-up vortices in the separated shear layer, due to the amplification of natural disturbances, are key in flow transition to turbulence. Huang et al. [39] also provide an insight in the vortex shedding modes of the NACA 0012 airfoil. These observed flow structures make correct two-dimensional evaluations of an LSB improbable.

Considering CFD simulations, RANS codes may capture the location of the laminar separation correctly if run without the turbulence model; however, they do not correctly model the flow after the laminar separation. This is due to the inability of RANS methods to model the transition from laminar to turbulent flow after laminar separation. Currently, the only way to correctly model the flow physics at these low Reynolds numbers is to use Direct Numerical Simulation (DNS). Unfortunately, the cost of DNS simulations is too prohibitive for the large number of simulations required to generate an airfoil database. For this reason, the possibility of laminar separation bubbles for this research will be solely based on estimated boundary layer properties.

ESTIMATION OF BOUNDARY LAYER STATE FOR CLF5605 AIRFOIL

The boundary layer state versus Reynolds number can now be evaluated. Figure 16 shows the predicted clf5605 airfoil boundary layer state for the upper side. The boundary layer is modeled as incompressible because of the large Reynolds number range.

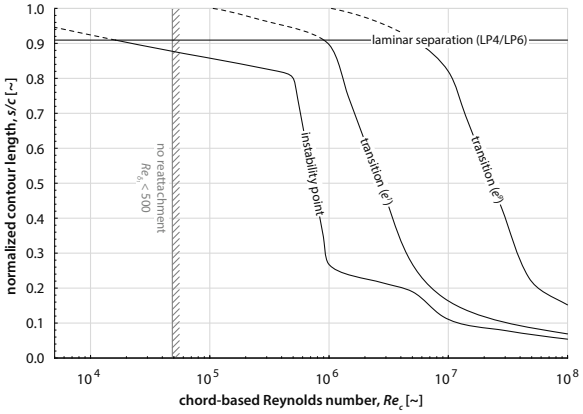

Figure 16. clf5605 upper surface boundary layer state versus Reynolds number ($\alpha = -3$)

The shape of the instability curve is characteristic for laminar flow airfoils. The pressure distribution can cause the limit of stability (see Figure 10) to have multiple unstable regions [19]. The most unfavorable case, instability in the earliest region, is plotted as the worst-case scenario. Instability in later regions is not evaluated. The transition estimates (for cumulative amplification equal to e^1 and e^9) tend to follow the shape of the instability curve. The chord-based Reynolds number at around $Re_c = 5 \cdot 10^4$ is where the boundary layer Reynolds number upon separation is lower than $Re_{\delta*} < 500$, making transition of separated laminar flow unlikely.

Figure 17 shows the boundary layer state for the same operating conditions, but for the pressure side of the clf5605 airfoil. The results show that for the clf5605 airfoil at $\alpha = -3$, even when including the expected accuracy of the point of laminar separation to be around 10%-chord [16], and the transition accuracy (at least when

the e^9 criterion is compared to experimental results) to be around 20% [30], turbulence transition on the blades is unlikely.

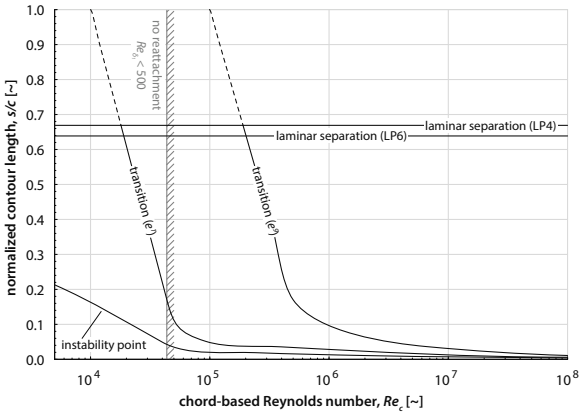

Figure 17. clf5605 lower surface boundary layer state versus Reynolds number ($\alpha = -3$)

ESTIMATION OF BOUNDARY LAYER STATE FOR THE MARS HELICOPTER IN HOVER

The rotor model from Grip et al. [2] is used in CAMRADII [41] to obtain the average angle of attack distribution of the MH rotor in hover for Mars Condition 2 at 2,800 RPM, shown in Figure D1 and Figure D2. The angle of attack for the outboard portion of the lower and upper rotor ranges between $\alpha = 0$ to $\alpha = 5$. The angle of attack is preferred over the section lift coefficient to avoid iterating the displacement thickness for effective camber losses upon lift convergence.

Evaluating the boundary layer at each CFD station for the angle of attack allows illustration of the estimated two-dimensional steady boundary layer state of the rotor, shown in Figure 18.

The rotor state from $r/R = 0.20$ to the root is linearly extrapolated because of the excessive airfoil thickness. The laminar separation (LP6) line is indicated by the shaded regions of suspected laminar separated flow. The boundary layer Reynolds numbers upon separation averages around $Re_{\delta*} = 300$ for the upper side, and $Re_{\delta*} = 160$ for the lower side, never exceeding $Re_{\delta*} = 500$. The upper side shows that the instability point is reached earlier and transition is unlikely.

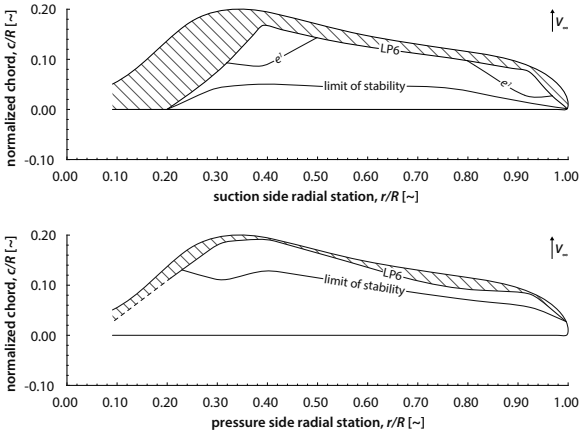

Figure 18. Mars Helicopter upper rotor, approximated compressible two-dimensional boundary layer state in hover for Mars Condition 2 at 2,800 RPM

To show the sensitivity for the e^n parameter, the e^1 total amplification rates are shown, for which local transition is just estimated to be possible. Figure 19 shows the estimated compressible two-dimensional boundary layer state for the lower rotor.

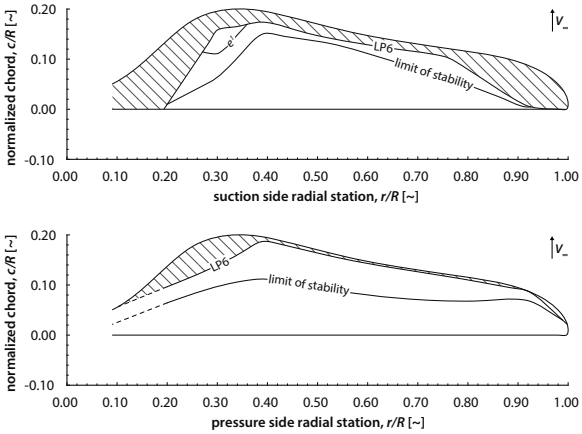

Figure 19. Mars Helicopter lower rotor, approximated compressible two-dimensional boundary layer state in hover for Mars Condition 2 at 2,800 RPM

The code predicts a tip with large regions of laminar separation because of the compressibility effects and higher angles of attack in the tip region compared to the upper rotor.

These results, although illustrative, must be interpreted as estimates at best due to the approximate nature of the methods described above, the sensitivity to changes in pressure distributions, and approximate evaluation of compressibility effects. In the absence of experimental data this is, however, used as an

estimation. Schmitz [15] elaborates on the difficulties of proper testing at these Reynolds number ranges and how to avoid 'false' transition in experiments.

The boundary layer state without compressibility effects is presented in Figure E1 and Figure E2. Evaluation of the same rotor RPM, in the Earth atmosphere, is presented in Figure E3 and Figure E4 to show the vast Reynolds number effects compared to the Martian atmospheric estimates. Transition is estimated to occur at an amplification factor equal to e^9 and no further evaluation of the turbulent boundary layer is pursued for Earth atmospheric conditions. Separation locations are predicted, but at much higher boundary layer Reynolds numbers, suggesting possible laminar separation bubbles. The boundary layer estimates indicate that for simulation of Martian atmospheric conditions, no transition model is needed, as the flow on the airfoil is laminar at the Reynolds number ranges investigated.

AIRFOIL SECTION CFD SIMULATIONS

A RANS-based approach using C81Gen is used to generate the aerodynamics coefficients for the airfoil deck. C81Gen is developed to create c81 format tables for a user-specified range of alpha-Mach pairs. C81Gen runs the two-dimensional, time-dependent compressible RANS solver ARC2D with structured body fitted viscous gridding. The program uses an implicit finite-difference method to solve two-dimensional thin-layer Navier-Stokes equations. C81Gen runs an alpha-Mach pair on each CPU core (or thread) available on a machine in parallel.

Within C81Gen, the flow type can be set to 'fully turbulent', 'fully laminar', or set to use pre-specified transition locations. C81Gen uses the Spalart-Allmaras (SA) turbulence model [42]. The SA turbulence model activates after $Re_c =$ 20,000 to 60,000, based on Mach number [43], and should not be used as (turbulence) transition model. The turbulence model was indeed found to not alter the results in the linear range of the coefficients for the Reynolds number ranges under consideration, but seemed to have a slight effect for the very high, stalled, angles of attack.

The time grid was chosen to be accelerated non-time accurate steady state with automatic switching to time-accurate if needed, based on residual values. In the case of a time-accurate simulation the coefficients will be based on the average of the periodic behavior.

For this study, C-grids where used and all airfoils had a normalized chord length of $c = 1.00$ with the far field located at $50c$. For the C-grid, the number of points in streamwise, normal, and wake direction are specified. The y^+ value was kept around $y^+ \approx 0.50$ for all cases investigated.

GRID RESOLUTION STUDY

An approximation of the numerical error is presented through a Grid Resolution Study (GRS). The absence of experimental results has also limited the GRS to roughly drag-count resolution. It was deemed further resolution –and therefore runtime- was not necessary until test results are available. The GRS was run for the clf5605 airfoil only, at $\mathrm{M} = 0.20, 0.40$, and 0.70. Table 5 shows the different grid settings used in the GRS.

Increasing grid density beyond grid 3 resulted in changes in drag below one drag count for $M =$ 0.70, which is the allowable accuracy of the coefficients in the c81 format. For the lower Mach numbers, slightly higher variation in minimum section drag was found, but it was concluded that grid 3 was of sufficient accuracy because in absence of test data that is beyond the confidence in any of the results. A close-up of grid 3 for the clf5605 airfoil is shown in Figure 20.

VALIDATION EFFORTS C81GEN

The C81Gen results are compared to two-dimensional OVERFLOW calculations using steady-state equations, with Low Mach Preconditioning and an SA turbulence model. Figure 21 shows the comparison between C81Gen and OVERFLOW. The main differences are observed outside the linear range, with drag differences in the linear range on the order of 10 drag counts. It is concluded that in the absence of test data the results are in close-enough agreement.

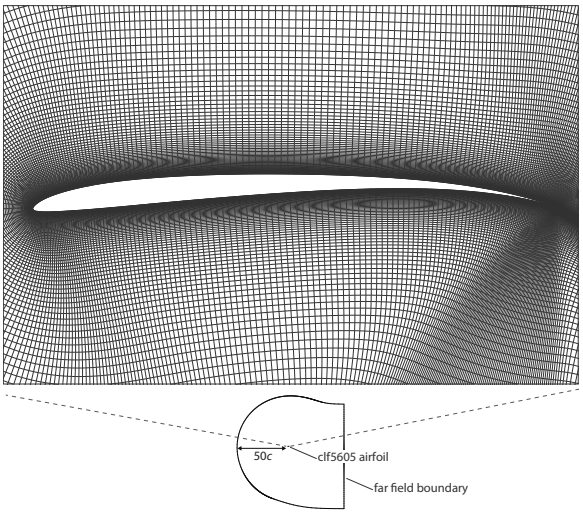

Figure 20. Close-up of C-grid for clf5605 airfoil

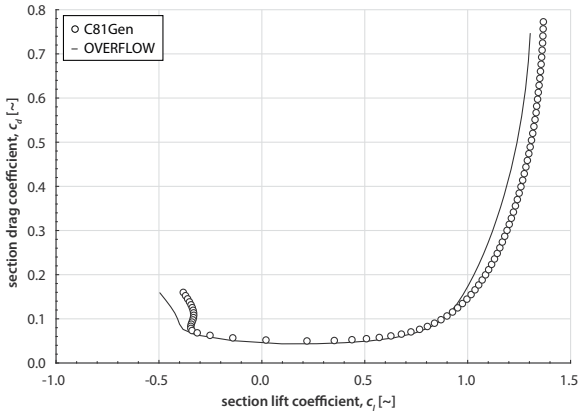

Figure 21. The lift-drag curve comparison between C81Gen and OVERFLOW for the CLF5605 airfoil at $T = 295\ K$, $M = 0.7$, and $Re_c = 7{,}600$

Table 5. Grid settings for the GRS

Grid	Streamwise points	Normal points	Wake points	y^+ ($M = 1.0$)
1	301	101	51	0.5
2	401	133	67	0.5
3	501	167	83	0.5
4	601	201	101	0.5
5	701	233	117	0.5
6	801	267	133	0.5
7	901	301	151	0.5
8	1101	367	183	0.5
9	1201	401	201	0.5

POST-PROCESSING AND RESULTS

C81Gen directly outputs c81-formatted files. A script processes the coefficient matrices, detects and removes anomalies, and stitches the data for very high angles of attack. The script stitches the airfoil files outside of the range simulated in C81Gen. The script was also used to make sure the coefficients were continuous over the whole angle of attack range. This process is repeated for all airfoils and all three Martian conditions. The stitching data was experimental data for a NACA 0012 airfoil. The angles of attack outside of the range simulated ($\alpha < -15$ or $\alpha > 20$), are not expected to occur in a region where large aerodynamic forces are expected. The user of the rotor model should be wary, however, to always observe the angle of attack distribution.

The lift curves for all Mach numbers for CFD Station 7 are presented as example in Figure F1 and Figure F2. The zero-lift section drag coefficients for all Mach numbers and CFD stations are computed and plotted over the results of Figure 6 and shown in Figure 22. The results show good agreement in general with Hoerner's experimental values at low Reynolds numbers obtained close to zero lift.

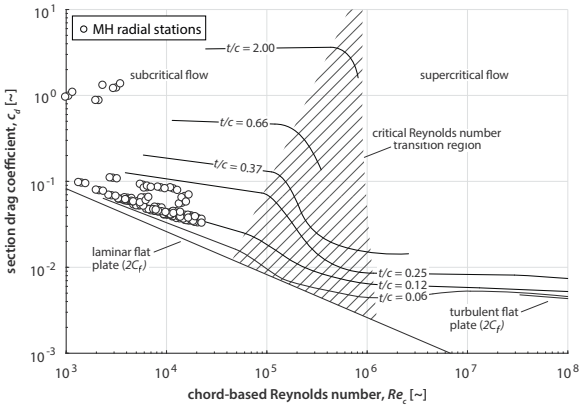

Figure 22. Reynolds number criticality based on thickness (close to zero section lift, created referring to Hoerner [13])

The maximum lift-to-drag ratio, maximum section lift, and minimum section drag are calculated for each case and plotted over the data presented by McMasters et al. [10] in Figure 23.

The maximum section lift-to-drag ratio shows the overlap between 'rough' airfoils and 'smooth' airfoils at the critical Reynolds number transition region. Below the Reynolds number transition rough airfoils can outperform smooth ones because the roughness induces transition of the boundary layer, delaying separation. The laminar airfoils of the MH outperform 'regular' smooth airfoils because of their ability to hold laminar flow for longer stretches. The maximum section lift is therefore also higher.

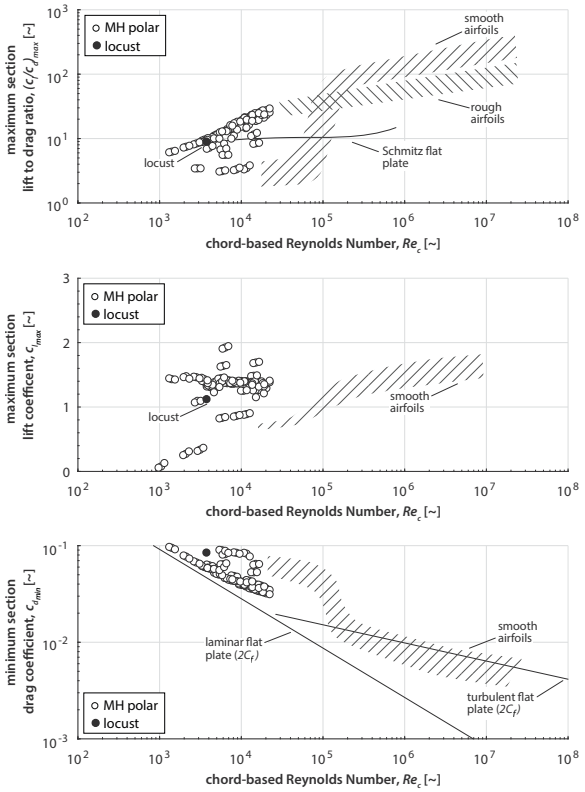

Figure 23. Effect of Reynolds number on airfoil performance (created referring to McMasters [10])

COMPARISON OF BOUNDARY LAYER STATE

Two cases are presented to investigate the flow field obtained from the CFD simulation and compare to the boundary layer predictions. Two stations are chosen for further inspection: an inboard region with substantial separated flow, and a section around the 3/4-radius location. The two chosen stations for hover are Station 3 ($r/R = 0.30, \alpha = 4.82, M = 0.22$) and Station 6 ($r/R = 0.76, \alpha = 3.01, M = 0.58$). They are compared using the C81Gen results for Station 3 at $\alpha = 5.00, M = 0.20$, and Station 6 at $\alpha = 3.00, M = 0.60$. The contour plots, showing non-dimensional density for Station 3 and Station 6, are shown in Figure F3 and Figure F4, respectively. The streamtraces for Station 3 and 6 are shown in Figure 24 and Figure 25, respectively.

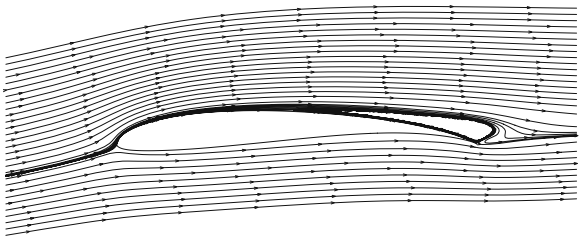

Figure 24. Streamtraces for Station 3, Mars Condition 2 ($r/R = 0.30, \alpha = 4.82, M = 0.22$)

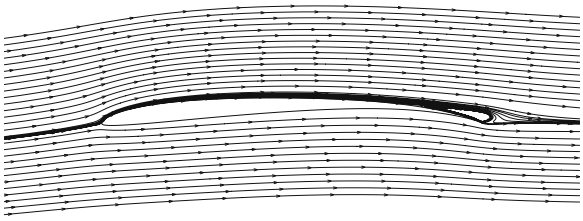

Figure 25. Streamtraces for Station 6, Mars Condition 2 ($r/R = 0.76, \alpha = 3.01, M = 0.58$)

Inspecting the local velocity vectors on the airfoil surface, it becomes possible to establish the location of separation. Station 3 shows separation at around $x/c = 0.44$. Station 6 shows laminar separation at around $x/c = 0.81$. Table 6 shows the comparison of the two stations under consideration, for the nearest angles of attack and Mach numbers simulated.

Table 6. Comparison of laminar separation locations

Station	Analytical	C81Gen	%-chord difference
3	0.36	0.44	8
6	0.87	0.81	6

The agreement is satisfactory and within the predicted accuracy of the method, disregarding the slight differences in operating conditions.

MARS HELICOPTER ROTOR PERFORMANCE

A free-wake analysis is performed with the obtained airfoil deck in CAMRADII to observe the isolated rotor performance of the MH. Figure 24 shows the computed Figure of Merit versus blade loading for all Martian Conditions. The plot includes a comparison with the chamber test measured performance from the 25ft Space Simulator at JPL.

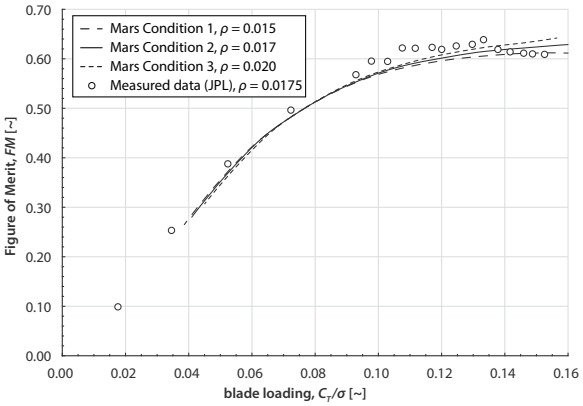

Figure 26. Figure of Merit versus blade loading for all Martian Conditions

The measured shaft power is obtained from motor power using a nearly constant motor/drive efficiency of 78%. The test data is obtained in CO_2 for slightly different flight conditions compared to the Martian Conditions, at $T = 288$ K and 2,600 RPM, but the correlation is satisfactory.

CONCLUSIONS & RECOMMENDATIONS

The goal of the present work is to create an aerodynamic rotor model for comprehensive analyses for the Mars Helicopter. The very low Reynolds number regime of the MH rotor in the Martian atmosphere is investigated and it is concluded a transition model is not necessary as the Reynolds number observed on the rotor in hover is subcritical with the flow remaining laminar on the airfoil. In the absence of test data, CFD simulations are compared with OVERFLOW calculations and various empirical data sources. The free-wake analysis in CAMRADII shows good agreement with the measured performance from the 25ft Space Simulator at JPL.

The spatial grid in C81Gen can be improved to have a higher cell density in the separated regions. Possible transonic (weak) shockwaves are currently not properly captured. A higher fidelity CFD simulation tool could provide more accurate results, particularly post stall, at the expense of more difficulty in the development of the c81 formatted files.

The boundary layer analysis can be improved to utilize more modern methods and assess the influence of the inherently three-dimensional flow over the rotor. Proper evaluation of laminar boundary layer-shock interaction should also be performed and its effect on the boundary layer stability and Tollmien-Schlichting waves should be evaluated.

Finally, airfoil tests are needed to further investigate this unexplored high Mach number, low Reynolds number research area for rotorcraft on Mars.

An in-depth description of the analyses in this paper can be found in the report by Koning [44].

ACKNOWLEDGEMENTS

The authors would like to thank William Warmbrodt, Alan Wadcock, and Gloria Yamauchi for their assistance and helpful discussions.

REFERENCES

[1] J. Balaram and P. T. Tokumaru, "Rotorcrafts for Mars Exploration," in *11th International Planetary Probe Workshop*, 2014.

[2] H. F. Grip *et al.*, "Flight Dynamics of a Mars Helicopter," in *43rd European Rotorcraft Forum*, 2017.

[3] J. (Bob) Balaram *et al.*, "Mars Helicopter Technology Demonstrator," in *AIAA Science and Technology Forum and Exposition (AIAA SciTech)*, 2018.

[4] L. A. Young and E. W. Aiken, "Engineering Studies into Vertical Lift Planetary Aerial Vehicles," in *AHS International Meeting on Advanced Rotorcraft Technology and Life Saving Activities*, 2002.

[5] L. A. Young, E. W. Aiken, M. Derby, R. Demblewski, and J. Navarrete, "Experimental Investigation and Demonstration of Rotary-Wing Technologies for Flight in the Atmosphere of Mars," in *58th Annual Forum of the AHS International*, 2002.

[6] K. J. Corfeld, R. C. Strawn, and L. N. Long, "Computational Analysis of a Prototype Martian Rotorcraft Experiment," in *AIAA Applied Aerodynamics Conference*, 2002.

[7] Jet Propulsion Laboratory, "Helicopter Could Be 'Scout' for Mars Rovers," 2015. [Online]. Available: https://www.jpl.nasa.gov/news/news.php?feature=4457. [Accessed: 12-Jun-2017].

[8] G. J. Leishman, *Principles of Helicopter Aerodynamics*, 2nd ed. New York: Cambridge University Press, 2006.

[9] A. Saxena, "Laminar Separation Bubble and Airfoil Design at Low Reynolds Numbers," 2008.

[10] J. H. McMasters and M. L. Henderson, "Low-Speed Single-Element Airfoil Synthesis," in *Third International Symposium on the Science and Technology of Low Speed and hide Motorless Flight*, 1979, pp. 19, 23.

[11] M. Drela, "Transonic low-Reynolds number airfoils," *Journal of Aircraft*, vol. 29, no. 6, pp. 1106–1113, Nov. 1992.

[12] M. Anyoji, D. Numata, H. Nagai, and K. Asai, "Effects of Mach Number and Specific Heat Ratio on Low-Reynolds-Number Airfoil Flows," *AIAA Journal*, vol. 53, no. 6, pp. 1640–1654, Oct. 2014.

[13] S. F. Hoerner, *Fluid-Dynamic Drag: Practical Information on Aerodynamic Drag and Hydrodynamic Resistance*. Hoerner Fluid Dynamics, 1965.

[14] S. F. Hoerner and H. V. Borst, *Fluid-Dynamic Lift: Practical Information on Aerodynamic and Hydrodynamic Lift*. Hoerner Fluid Dynamics, 1985.

[15] F. W. Schmitz, "Aerodynamics of the model airplane. Part 1 - Airfoil measurements," Huntsville, Alabama, 1967.

[16] K. Bussmann and A. Ulrich, "Systematic Investigations of the Influence of the Shape of the Profile Upon the Position of the Transition Point," Washington, D.C., 1947.

[17] T. J. Mueller, *Fixed and Flapping Wing Aerodynamics for Micro Air Vehicle Applications*. American Institute of Aeronautics & Astronautics, 2001.

[18] J. Winslow, H. Otsuka, B. Govindarajan, and I. Chopra, "Basic Understanding of Airfoil Characteristics at Low Reynolds Numbers," in *7th AHS Technical Meeting on VTOL Unmanned Aircraft Systems*, 2017.

[19] H. Schlichting and J. Kestin, *Boundary-Layer Theory*, 6th ed. 1968.

[20] K. Pohlhausen, "Zur Näherungsweisen Integration der Differentialgleichung der Laminaren Grenzschicht," *Zeitschrift für Angewandte Mathematik und Mechanik*, vol. 1, no. 4, pp. 252–290, Jan. 1921.

[21] H. Holstein and T. Bohlen, "Ein einfaches Verfahren zur Berechnung Laminarer Reibungs-schichten die dem Naherungsverfahren von K. Pohlhausen genugen," 1940.

[22] H. Schlichting and J. Kestin, *Boundary-Layer Theory*, 7th ed. 1979.

[23] A. Walz, "Ein neuer Ansatz fur das Geschwindigkeitsprofil der Laminaren Reibungsschicht," *Lilienthal-Bericht 14J*, pp. 8–12, 1941.

[24] M. Drela, "XFOIL: An Analysis and Design System for Low Reynolds Number Airfoils," in *Conference on Low Reynolds Number Airfoil Aerodynamics*, 1989.

[25] M. Hepperle, "JAVAFOIL User's Guide." 2017.

[26] H. Schlichting and A. Ulrich, "On the Calculation of the Transition Laminar/Turbulent," *Jahrb d. DL I*, p. 8, 1942.

[27] J. Pretsch, "The Stability of a Two-Dimensional Laminar Flow in Pressure Drop and Pressure Rise," *Jahrb d. DL I*, p. 58, 1941.

[28] J. Pretsch, "The excitation of unstable perturbations in a laminar friction layer," 1952.

[29] A. R. Wazzan, T. T. Okamura, and A. M. O. Smith, "Spatial and Temporal Stability Charts for the Falkner-Skan Boundary-Layer Profiles," 1968.

[30] A. M. O. Smith, "Transition, Pressure Gradient, and Stability Theory.," El Segundo, California, 1956.

[31] J. van Ingen, "A Suggested Semi-Empirical Method for the Calculation of the Boundary Layer Transition Region," Delft, the Netherlands, 1956.

[32] F. W. Boltz, G. C. Kenyon, and C. Q. Allen, "Measurements of Boundary-layer Transition at Low Speed on Two Bodies of Revolution in a Low-turbulence Wind Tunnel," Moffett Field, California, 1956.

[33] A. L. Braslow and F. Visconti, "Investigation of Boundary-layer Reynolds Number for Transition on an NACA 65(215)-114 Airfoil in the Langley Two-dimensional Low-turbulence Pressure Tunnel," Langley Field, Virginia, 1948.

[34] R. Vos and S. Farokhi, *Introduction to Transonic Aerodynamics*. Delft: Springer, 2015.

[35] J. Laufer and T. Vrebalovich, "Stability and transition of a supersonic laminar boundary layer on an insulated flat plate," *Journal of Fluid Mechanics*, vol. 9, no. 2, p. 257, Oct. 1960.

[36] B. H. Carmichael, "Low Reynolds Number Airfoil Survey, Volume 1," Capistrano Beach, California, 1981.

[37] M. O'Meara and T. J. Mueller, "Laminar separation bubble characteristics on an airfoil at low Reynolds numbers," *AIAA Journal*, vol. 25, no. 8, pp. 1033–1041, Aug. 1987.

[38] W. Shyy, Y. Lian, J. Tang, D. Viieru, and H. Liu, *Aerodynamics of Low Reynolds Number Flyers*. Cambridge University Press, 2007.

[39] R. F. Huang and C. L. Lin, "Vortex shedding and shear-layer instability of wing at low-Reynolds numbers," *AIAA Journal*, vol. 33, no. 8, pp. 1398–1403, Aug. 1995.

[40] S. Yarusevych, P. E. Sullivan, and J. G. Kawall, "On vortex shedding from an airfoil in low-Reynolds-number flows," *Journal of Fluid Mechanics*, vol. 632, p. 245, Aug. 2009.

[41] W. Johnson, "CAMRAD II Comprehensive Analytical Model of Rotorcraft Aerodynamics and Dynamics." Johnson Aeronautics, Palo Alto, 2005.

[42] P. Spalart and S. Allmaras, "A one-equation turbulence model for aerodynamic flows," in *30th Aerospace Sciences Meeting and Exhibit*, American Institute of Aeronautics and Astronautics, 1992.

[43] C. L. Rumsey and P. R. Spalart, "Turbulence Model Behavior in Low Reynolds Number Regions of Aerodynamic Flowfields," in *38th AIAA Fluid Dynamics Conference and Exhibit*, 2009, p. 5.

[44] W. J. F. Koning, "Mars Helicopter Rotor Aerodynamics and Modeling," NASA CR-2018-219735, Moffett Field, California, 2018.

[45] K. Lodders and B. Fegley, Jr., *The Planetary Scientist's Companion*. Oxford University Press, 1998.

[46] A. R. Wazzan, T. T. Okamura, and A. M. O. Smith, "Stability of Laminar Boundary Layers at Separation," *American Institute of Physics*, vol. 10, 1967.

APPENDIX A
MARTIAN ATMOSPHERIC COMPOSITION

The composition of the Martian atmosphere is presented in Table A1.

Table A1. Mars atmospheric composition comparison [45]

Gas	Earth	Mars
O_2 (oxygen)	21%	0.1%
CO_2 (carbon dioxide)	< 0.1%	95%
N_2 (nitrogen)	78%	2.7%
Ar (argon)	0.9%	1.6%
Others	0.1%	0.6%

APPENDIX B
ROTOR PARAMETERS

Figure B1 shows the chord, thickness, and twist distribution for the MH rotor. Figure B2 shows the normalized airfoil cross sections for the MH rotor. The thickness and camber properties of the airfoils are presented in Table B1.

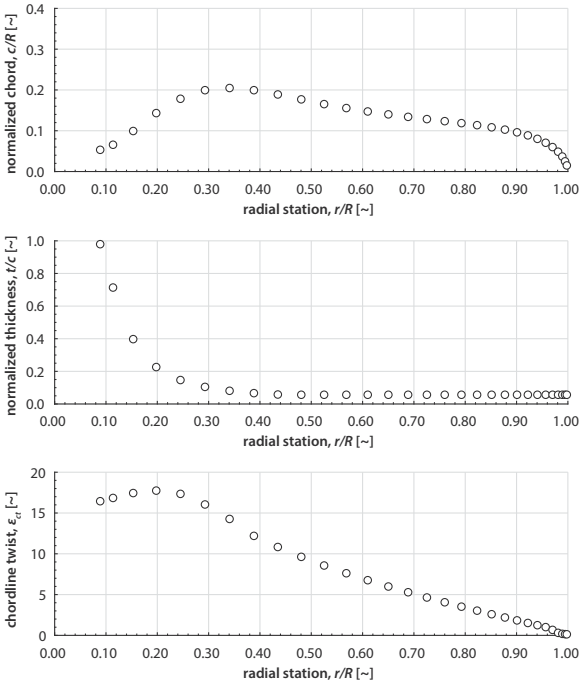

Figure B1. The chord, thickness, and twist distribution for the MH rotor

Table B1. MH Airfoil thickness and camber details

Airfoil	t/c [~]	$x_{t/c}$ [x/c]	f/c [~]	$x_{f/c}$ [x/c]
Station 1	96.201	0.466	0.000	0.000
Station 2	21.985	0.346	5.298	0.594
Station 3	9.800	0.255	5.083	0.591
Station 4	5.899	0.201	4.944	0.597
clf5605	5.000	0.200	4.910	0.593

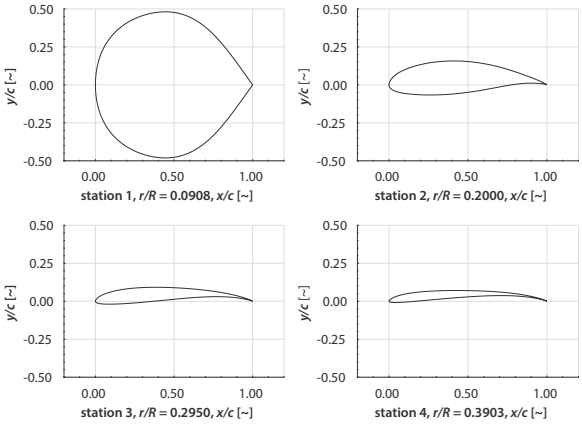

Figure B2. The normalized airfoil profiles for the MH rotor

APPENDIX C
LAMINAR SEPARATION PREDICTION

Table C1 shows the comparison of the laminar separation locations of the present work with the work by Bussmann et al. [16].

Table C1. Theoretical laminar separation points (LP6 criterion), comparison Walz linearization with Bussmann et al.

Airfoil	Source	c_l	0.00	0.25	0.50	0.75	1.00
J025	Present work	S	0.396	0.351	0.311	0.282	0.246
		P	0.394	0.439	0.495	0.543	0.604
	[16]	S	0.403	0.353	0.308	N/A	0.252
		P	0.403	0.435	0.491	N/A	0.592
J415	Present work	S	0.675	0.617	0.558	0.499	0.433
		P	0.142	0.224	0.329	0.465	N/A
	[16]	S	0.686	0.630	0.570	N/A	0.476
		P	0.200	0.283	0.377	N/A	0.494
J815	Present work	S	0.749	0.709	0.674	0.635	0.597
		P	0.039	0.048	0.072	0.116	0.189
	[16]	S	0.737	0.685	0.648	N/A	0.594
		P	0.043	0.056	0.093	N/A	0.192

APPENDIX D
ROTOR STATE CAMRADII

The averaged angle of attack distribution on the MH rotor in hover obtained from CAMRADII is shown in Figure D1 and Figure D2. The error bar length represents 2σ.

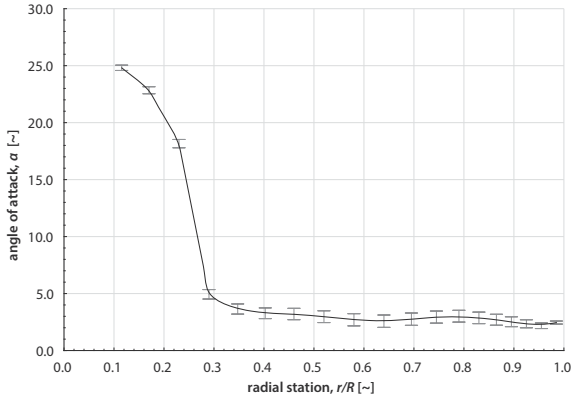

Figure D1. Upper rotor average angle of attack distribution over azimuth in hover from CAMRADII

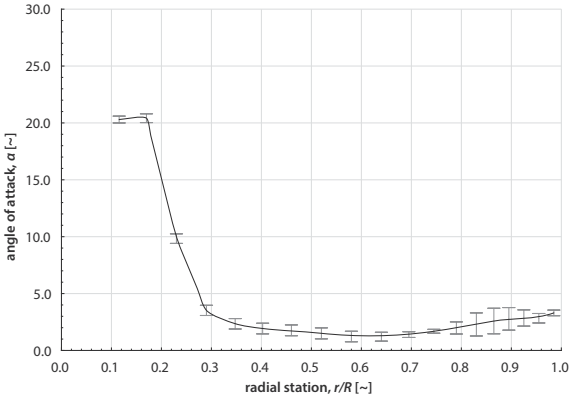

Figure D2. Lower rotor average angle of attack distribution over azimuth in hover from CAMRADII

APPENDIX E
BOUNDARY LAYER STATE

Figure E1 to Figure E4 show the estimated boundary layer state for the MH in hover for incompressible flow on Mars and compressible flow on Earth.

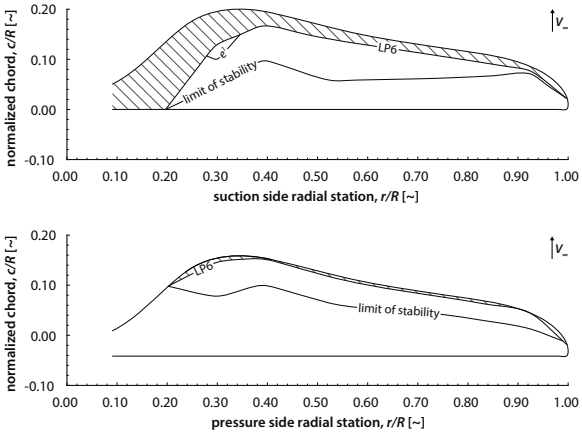

Figure E1. Mars Helicopter upper rotor, approximated incompressible two-dimensional boundary layer state in hover for Mars Condition 2 at 2,800 RPM

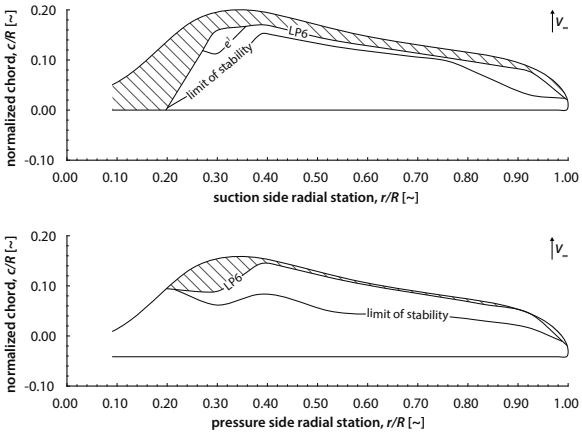

Figure E2. Mars Helicopter lower rotor, approximated incompressible two-dimensional boundary layer state in hover for Mars Condition 2 at 2,800 RPM

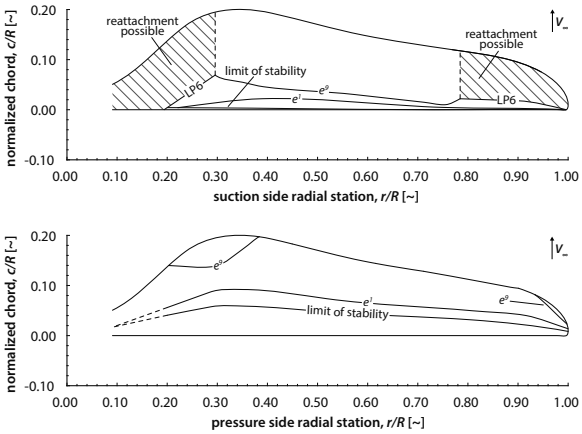

Figure E3. Mars Helicopter upper rotor, approximated compressible two-dimensional boundary layer state in hover on Earth at 2,800 RPM

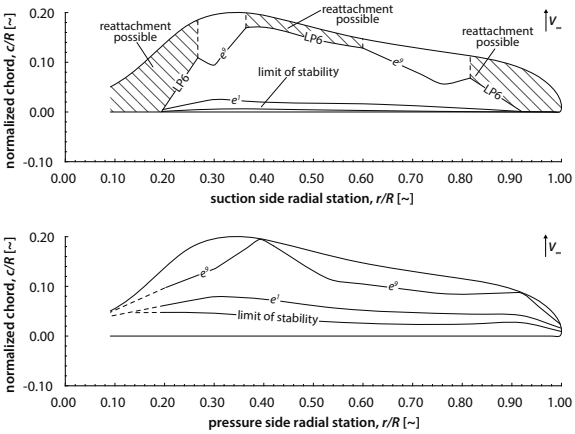

Figure E4. Mars Helicopter lower rotor, approximated compressible two-dimensional boundary layer state in hover on Earth at 2,800 RPM

APPENDIX F
CFD RESULTS

Figure F1 and Figure F2 show the lift curve and the drag coefficients at Station 7 for various Mach numbers simulated. Figure F3 and Figure F4 show the non-dimensional density contours for Station 3 and 6, respectively.

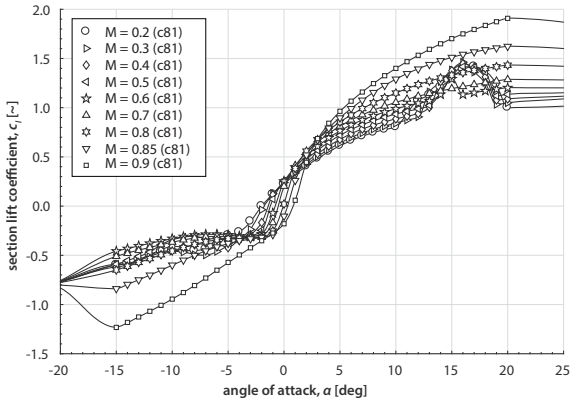

Figure F1. The lift curves for the clf5605 airfoil at Station 7 for various Mach numbers

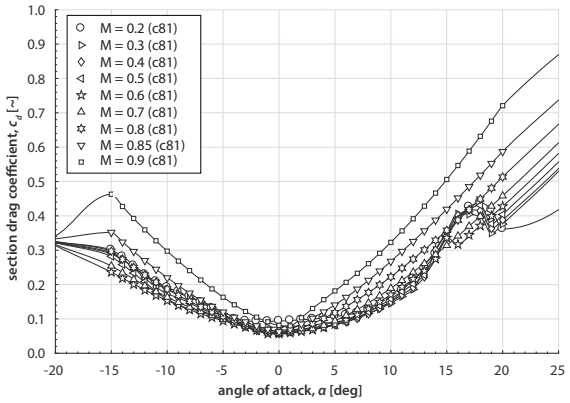

Figure F2. The drag polars for the clf5605 airfoil at Station 7 for various Mach numbers

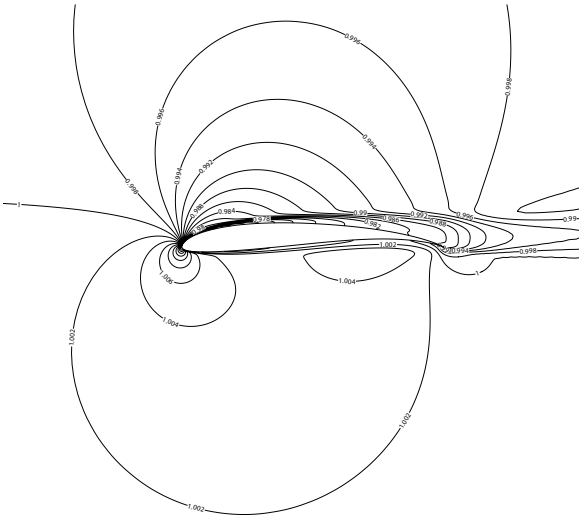

Figure F3. Non-dimensional density contours, ρ/ρ_∞ for Station 3, Mars Condition 2 ($r/R = 0.30, \alpha = 4.82, M = 0.22$)

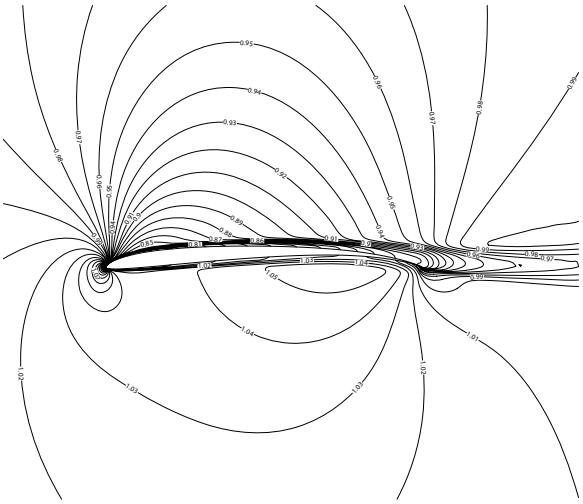

Figure F4. Non-dimensional density contours, ρ/ρ_∞ for Station 6, Mars Condition 2 ($r/R = 0.76, \alpha = 3.01, M = 0.58$)